A numerical and analytical study of the effect of aspect ratio on the behavior of a round thermal

A numerical and analytical study of the effect of aspect ratio on the behavior of a round thermal

Adrian C.H. Lai[1], Bing Zhao[2], Adrian Wing-Keung Law[3], and E. Eric Adams[4]

Abstract: A round thermal is formed when an element of buoyant fluid is released instantaneously into a quiescent ambient. Although the thermal spreading rate is of primary importance to mathematical modeling, the reported values in the literature vary greatly. To identify possible factors affecting the thermal spreading rate, we investigated the effect of different initial conditions numerically by solving the unsteady Reynolds-averaged Navier-Stokes equations with a two-equation turbulence closure. The initial aspect ratio (i.e. length-to-diameter ratio) of the thermal was varied between 0.125 – 4.0, and the initial density differences was changed from 1% to 10%. Results show that the spreading rate is greatly affected by the initial aspect ratio, which also explains the variations in earlier reported values.

Following the numerical study, an analytical model using buoyant vortex ring theory is developed to predict the spreading rate of a thermal. The predictions show good agreement with the results from both the numerical simulations and previous experimental studies. Another simple analytical model is also presented to approximate the thermal induced flow, and is validated using the numerical simulations.

Keywords: buoyant vortex rings; thermals; Norbury vortex; Hill's vortex; formation number; spreading rate; entrainment coefficient

1Center for Environmental Sensing and Modeling, Singapore-MIT Alliance for Research and Technology Centre, 1 CREATE Way, Singapore 138602. Email: adrian.lai@smart.mit.edu

2 School of Civil and Environmental Engineering, Nanyang Technological University, 50 Nanyang Avenue, 639798 Singapore. Email: zhao0129@e.ntu.edu.sg

3 School of Civil and Environmental Engineering, Nanyang Technological University, 50 Nanyang Avenue, 639798 Singapore. Email: cwklaw@ntu.edu.sg

4 Department of Civil and Environmental Engineering, Massachusetts Institute of Technology, Cambridge, MA 02139, USA. Email: eeadams@mit.edu

1 Introduction

A thermal is formed when an element of positively or negatively buoyant fluid is released instantaneously into a quiescent ambient. The phenomenon can be observed in many environmental fluid mechanics problems, including the convection of cumulus clouds (Scorer 1957, Woodward 1959), sediment cloud releases for land reclamation or dredging (e.g. Ruggaber and Adams 2001, Zhao et al. 2012), and the transport of virus droplets by hot air (Lee and Chu 2003). The thermal is characterized by a vortex-ring like structure carrying an approximately ellipsoidal shape of fluid/tracer (Figure 1), and it grows with time due to the entrainment of external ambient fluid which also causes changes to other transient characteristics such as the rise or decent velocity.

The spreading rate is an important parameter that determines the thermal's transient characteristics. In the integral model proposed by Turner (1963), the entrainment rate could be inferred from the experimental measurements of thermal spreading rate. The conservation of volume, momentum, and buoyancy equations of the thermal were then solved based on the entrainment hypothesis (Morton et al. 1956) to predict the development of thermal with time. There were later many extensions to the model with additional effects being accounted for. For example, Escudier and Maxworthy (1973) included the added mass and drag force into the equations, leading to a more consistent formulation. Several studies in the context of two-phase particle thermals, further extended the integral model to account for the linear ambient density stratification (Bush et al. 2003), release height effects (Zhao et al. 2012), and buoyancy reduction effects (Lai et al. 2013).

As far as the model parameters are concerned, Ruggaber (2000) showed that in general the model prediction is most sensitive to the spreading rate, while added mass and drag force could be considered secondary.

The measured thermal spreading rate varied greatly among different studies in the literature. Scorer (1957) first reported the thermal spreading rate to be about 0.25 (with a range of 0.15 – 0.4 depending on the buoyant fluid release speed). Escudier and Maxworthy (1973) indicated that in some cases it can be as small as 0.10, while suggesting a normal value of 0.25. Recent well-controlled experiments by Hart (2008), Bond and Johari (2005, 2010), and Zhao et al. (2013) also reported different results, ranging from about 0.15 – 0.25. The qualitative reasons for the differences were often attributed to initial disturbances during the release, and the instability of the thermal itself.

Recent experiments have focused on further details of the thermal. For example, the aspect ratio (length to diameter) effect was investigated by Bond and Johari (2005) with L/D of 2 – 8; within this range the thermal characteristics were unaffected by the initial geometry. The structure of ensemble-averaged internal vorticity and density distributions were obtained by Zhao et al. (2013). A few numerical studies have also been carried out. Lundgren et al. (1992)'s vortex method focused on the region close to the source, and Li and Ma (2003)'s large eddy simulations demonstrated the effect of initial disturbance on the thermal's development, with a fixed aspect ratio of the initial release equal to unity.

In this paper, we conduct a systematic numerical investigation on the transient development of the thermal by solving the unsteady Reynolds-averaged Navier-

Stokes (RANS) equation with a two-equation turbulence closure. In the following, we shall show that a key factor affecting the thermal's spreading rate is the aspect ratio of the source. Using both the numerical results and buoyant vortex ring theory, we then develop the quantitative link between the spreading rate and initial aspect ratio, and validate the relationship using data in the literature. Implications from this study that are useful in engineering applications are also discussed.

2 Numerical simulations of a round thermal

2.1 Problem definition

The configuration being considered is illustrated in Figure 2. A small cylindrical volume V_o of buoyant fluid centered at $(z, r) = (0, 0)$ of length L and diameter D with density ρ_o , is released from rest into an unbounded quiescent ambient of density ρ_a. The buoyancy of the fluid $F_o = (\Delta\rho_o / \rho_a)gV_o$ ($\Delta\rho_o$ = density difference between the fluid and the ambient $\rho_o - \rho_a$; g = acceleration due to gravity) drives the fluid upward to form a thermal, with a buoyant vortex ring core carrying a roughly ellipsoidal buoyant fluid. The thermal size increases during its rise due to the entrainment of surrounding ambient fluid. The distance from the vertical axis to the vortex ring core is r_r with the corresponding height z_r; the distance to the maximum thermal radius is r_m with height z_m. The maximum thermal rise height is denoted by z_f. The main objective is to determine the spreading rate of the thermal, $\alpha_m = dr_m/dz_m$, under different initial conditions. The spreading rate of the ring, $\alpha_r = dr_r/dz_r$, and the spreading rate as defined in many experimental studies, $\alpha_e = dr_m/dz_f$,can be related to α_m by a constant.

2.2 Governing equations

Numerical simulations were carried out to simulate thermal releases with various initial aspect ratios. The thermal characteristics were computed by solving the unsteady Reynolds-averaged Navier-Stokes equations (RANS) using a Cartesian finite volume open source code OpenFOAM (Weller et al. 1998). The standard *k*-ε turbulence closure (Launder and Spalding 1974) was used. A 'two-liquid mixing' model (OpenFOAM Foundation 2010) was adopted to account for the mixing between the source and ambient fluids; the buoyancy effect was incorporated in the two-equation model using Rodi (1987)'s formulation. The governing equations include the following:

$$\frac{\partial \rho}{\partial t} + \nabla \cdot (\rho \vec{u}) = 0 \tag{1}$$

$$\frac{\partial (\rho \vec{u})}{\partial t} + \vec{u} \nabla \cdot (\rho \vec{u}) = -\nabla p + \rho \vec{g} + \nabla^2 (\mu_t \vec{u}) \tag{2}$$

$$\frac{\partial (\rho \phi_o)}{\partial t} + \vec{u} \nabla \cdot (\rho \phi_o) = \nabla^2 (\frac{\mu_t}{Sc_t} \rho \phi_o) \tag{3}$$

$$\frac{\partial k}{\partial t} + \vec{u} (\nabla \cdot k) = \nabla^2 (\frac{v_t}{\sigma_k} k) + P + G - \varepsilon \tag{4}$$

$$\frac{\partial \varepsilon}{\partial t} + \vec{u} (\nabla \cdot \varepsilon) = \nabla^2 (\frac{v_t}{\sigma_\varepsilon} k) + C_{1\varepsilon} \frac{\varepsilon}{k} (P + C_{3\varepsilon} G) - C_{2\varepsilon} \frac{\varepsilon^2}{k} \tag{5}$$

$$\rho = \phi_o \rho_o + (1 - \phi_o) \rho_a \tag{6}$$

$$\mu_{eff} = \phi_o \mu_o + (1 - \phi_o) \mu_a \tag{7}$$

where $\vec{u}$ is the velocity vector; ρ is the fluid density; p is pressure; μ_t is the dynamic eddy viscosity; v_t is the effective kinematic eddy viscosity; φ is the volume fraction; k is the kinetic energy and ε is the energy dissipation rate. Subscripts o and a denote the buoyant and ambient fluids respectively.

Kinetic energy is produced by the shear production term P and the buoyancy production term G in the k-equation (4), where

$$P = \nu_t \left(\frac{\partial u_i}{\partial x_j} + \frac{\partial u_j}{\partial x_i}\right)\frac{\partial u_i}{\partial x_j} \quad \text{and} \quad G = -g_i \frac{\nu_t}{\rho S_{ct}} \frac{\partial \rho}{\partial x_i}.$$

The eddy viscosity is

$$\nu_t = C_\mu \frac{k^2}{\varepsilon}.$$

The turbulence coefficients adopted are: $C_\mu = 0.09$; $C_{1\varepsilon} = 0.09$; $C_{2\varepsilon} = 1.92$; $C_{3\varepsilon} = 0.8C_{1\varepsilon}$ for $G > 0$ (unstably stratified flows) and $C_{3\varepsilon} = 0$ for $G<0$ (stably stratified flows). $\sigma_k = 1.0$; $\sigma_\varepsilon = 1.3$; and the turbulent Schmidt number is $S_{tc} = 0.7$. These values are commonly adopted in the literature.

Among the empirical coefficients above, note that $C_{3\varepsilon}$ is dependent on the flow type (Rodi 1987). We find that this constant can affect the simulated results (to be discussed in Section 3.5.2.). A larger $C_{3\varepsilon}$ generally leads to a smaller spreading rate, and we obtained an optimal value by comparison with previous round thermal experiments. By so doing, any 'imperfect' experimental conditions, such as the boundary layer effect from the cylindrical tube, will also be implicitely accounted for in the simulations.

2.3 Initial and boundary conditions

In order to use a Cartesian solver in our cylindrical problem, the physical domain of the simulation was made to have a 'wedge' shape of one cell thick (Figure 3), subtending an angle <5^o, making the computation effectively two-dimensional with cylindrical coordinates (OpenFOAM Foundation 2010). The results reported herein were in (r, z), where r is the radial direction and z the vertical direction. A total of 200 x 600 uniform cells were used to discretize the domain which is 0.15

m wide and 0.8 m tall. Doubling the width of the physical domain was shown to result in a typical difference in spreading rate of less than 5%. The total grid number was chosen after a grid independency check which will be discussed in later sections.

On the top, bottom, and the arc surface of the cylindrical domain, a zero pressure boundary condition was imposed, while a zero gradient boundary condition was specified for other quantities. The remaining two faces were in rotational symmetry. Initially, a cylindrical patch (shaded in Figure 3) representing the buoyant fluid was given a density ρ_o (volume fraction $\alpha_1 = 1$) producing a density difference of $\Delta\rho_o$ with the ambient fluid from 1% - 10%. The diameter D of the buoyant fluid ranged from 1.8 cm – 3.7 cm, and its length L from 0.125 – 4.0D. The release parameters for all cases considered are tabulated in Table 1. In particular, the cases D5LD2 and D3LD05 corresponded directly to the experiments of Zhao et al. (2013) and Hart (2008) respectively.

A small disturbance was introduced via the initial turbulent kinetic energy (and its dissipation computed accordingly) of the fluid to prevent unrealistic initial eddy viscosity. The resulting initial values of k and ε in the buoyant patch can be estimated to be of order of 1.0E-05 m^2/s^2 and 1.0E-05 m^2/s^3 respectively by assuming homogeneous velocity fluctuation in all directions. The k and ε of the ambient fluid were set to be 0.01% of the corresponding values for the buoyant patch – which was essentially non-turbulent. The results were not noticeably affected by the choice of k within a reasonable range, as long as ε was chosen appropriately (in general $\varepsilon = C_\mu^{3/4} k^{3/2}/l$, where l is a characteristic length of order $0.1D$).

2.4 Computational details

Equations (1) – (7) were solved numerically using OpenFOAM. A collocated arrangement was used for all dependent variables (Jasak 1996). The values at the face center of a control volume were obtained by linear interpolation. A number of schemes were used in discretizing the equations. For the Laplacian terms, a linear scheme was adopted, while for the convection terms, a MUSCL scheme was adopted. A Crank-Nicolson scheme was used for time-discretization. In solving the equation matrices, a preconditioned conjugate gradient solver was used for p, u, k, and ε; and a smoother is used for φ_1. The solution tolerance for these variables ranged from 1E-06 to 1E-08 for convergence. The pressure-implicit split operator (PISO) algorithm was used in the iterative procedures for solving the equations for velocity and pressure. The details of the solution procedures can be found in Jasak (1996).

3 Results from numerical simulations

3.1 Comparison with experiments

To ensure the reliability of the simulation, we first compared the results of the numerical simulations with experimental results reported in the literature. Zhao et al. (2013)'s and Hart (2008)'s experiments of a negatively buoyant round thermal released from a cylinder were chosen, since they were well documented with careful attention paid to the control of initial conditions. Note that we inverted their results upside down for better presentation, which was justified within the limits of the Boussinesq approximation.

3.1.1 Thermal gross characteristics

The release conditions of Zhao et al. (2013)'s study were: D = 1.8 cm, L/D = 2, and $\Delta\rho/\rho$ = 5%; while those for Hart (2008)'s study were D = 3.7 cm, L/D = 0.5, and $\Delta\rho/\rho$ = 3%. The numerically simulated thermal gross characteristics are compared with experiments in Figure 4. Figure 4(a) shows the thermal spreading rate, defined using the maximum thermal radius, i.e. normalized concentration contour C/C_m = 0.05 (maximum difference in using C/C_m = 0.01 – 0.1 is in the order of 5%), where C and C_m are the concentration field and local maximum concentration, respectively; also note that the density field and the concentration field were actually inferred from the volume fraction) divided by the corresponding height. The numerically predicted α_e = 0.13 was in good agreement with the average of the best 15 experimental runs with α_e = 0.16 obtained by Zhao et al. (2013), and the numerically predicted α_e = 0.27 was also in good agreement with the experimental α_e = 0.25 obtained by Hart (2008). Figure 4(b) compares the transient height variation of the thermal, where time is normalized by the thermal characteristic time defined in Zhao et al. (2013) as $T_{MT} = F_o^{1/6}/g^{2/3}$. Again, the numerical simulation was able to reproduce both set of experiments well. Comparing the thermal characteristics in these two studies, it was apparent that a higher initial aspect ratio leads to smaller thermal growth rate.

As seen in Figure 5 (a) and (b), there is visually no difference in the time history of the thermal growth and also its rise height by varying the initial density difference, as long as the initial aspect is kept fixed. The effect of changing initial density difference on the gross thermal characteristics is thus small.

3.1.2 Thermal internal structure

Further comparisons were made of the internal structure of a thermal using Zhao et al. (2013)'s experimental data. Figure 6(a) shows the simulated and observed concentration profile along $z = z_r$. The simulated profile of $z \approx 10D$ (no significant difference for 8 – 12D) in general agreed well with experimental data, except that the experimental data appeared more 'diffused' near the thermal edge. Note that the experimental data from Zhao et al. (2013) represented an ensemble average of 15 runs, and some of the runs might deviate from the axisymmetric axis, which offered a possible reason for the deviation. Figure 6(b) plots the simulated and observed vorticity profiles, where the comparison is similar to that of the concentration profiles. We have examined the concentration and vorticity profiles obtained from the same release but with initial density difference of 1% and 10% (not shown). The results showed virtually no noticeable difference from those with 5%.

3.2 General observations from numerical simulations

The comparison with both Zhao et al. (2013) and Hart (2008) was generally agreeable. This verified that the numerical simulations should be able to represent the ensemble average of a round thermal reasonably well. The effect of initial release aspect ratio was then further explored by numerical simulations. The simulated normalized concentration distributions (or density difference distributions) with initial aspect ratios 0.5 – 3.0 are shown in Figures 7(a) – (d). The contours are obtained after the thermal has become self-similar (which was confirmed when the normalized concentration distribution showed no noticeable difference over time), and are normalized by their local maximum concentration. As L/D increased from 0.5 – 2.0, it can be seen that more and more buoyant fluid

was being carried by the buoyant vortex ring, leading to an increase in the buoyant vortex ring thickness. Starting from L/D = 2.0, there was apparently a thin trailing stem being ejected from the thermal, indicating that the buoyant ring had already attained the maximum volume of fluid that it can carry. Further increasing the aspect ratio beyond this point did not increase the thickness of the ring, but resulted in more buoyant fluid being ejected as evidenced in the case of L/D = 3.0. Figures 7(e) – (h) show the normalized vorticity contours of a round thermal with L/D = 0.5 – 3.0. The contours are similar to the concentration contours although their shape is slightly different. The ring thickness increased with an increase in aspect ratio up to 2.0, then a trailing stem was formed if the ratio was further increased. As the flow characteristics of a vortex ring are controlled by its vorticity distribution, it is natural to assume that the thermal's characteristics are dependent on its initial aspect ratio for L/D < 2.

The contour plots of the normalized turbulent kinetic energy k and its dissipation rate ε are shown in Figures 8(a) – (d), and Figures 8(e) – (h) respectively. Similar to the concentration contours, the k contours in general had a flatter shape as L/D decreased, and no further change beyond L/D = 2. For all cases, the maximum k occurred near the front of the rising thermal. The characteristic double peaks seen in both the concentration and vorticity contours no longer appeared when L/D > 1. The ε contours looked similar to those of k, including the maximum at the thermal front.

3.3 The spread of a thermal

Using a maximum radius defined by the normalized concentration contour of 0.05, the ring radius of selected thermals versus height is shown in Figure 9. Figure 9(a) shows the spreading rate of the thermal with $\Delta\rho/\rho = 3\%$ and D = 3.7

cm. The rate generally increased with decreasing initial aspect ratio (from 0.13 when L/D = 2 to 0.34 when L/D = 0.125), although the difference between L/D = 0.25 and 0.5 was less distinct. Figure 9(b) shows the case of $\Delta\rho/\rho$ = 5% and D = 1.8 cm. Again, the spreading rate increased with decreasing aspect ratio (0.15 – 0.21). Increasing the aspect ratio beyond 2 did not have any noticeable effect on the thermal spread. This is to be expected from the previous discussion as beyond an L/D of 2, no more buoyant fluid can be incorporated into the thermal to alter its internal structure. The spreading rate was also less affected by parameters other than L/D. For example, increasing the total buoyancy by 5 times while keeping L/D unchanged led to a maximum variation of only 15% in the spreading rate. Most importantly, by solely adjusting the initial aspect ratio in this study, we were able to reproduce the range (0.13 – 0.31) of spreading rate reported among the different studies in the literature. This suggests that the initial aspect ratio could be the key parameter that leads to the variations.

3.4 Asymptotic circulation

It has been reported in the literature that the normalized asymptotic baroclinic circulation $\Gamma/F_o^{1/2}$ that a round thermal can attain is a constant. In particular, for L/D > 2, both experimental results (Bond and Johari 2010; Zhao et al. 2013) and theoretical predictions (Lundgren et al. 1992) showed that $\Gamma/F_o^{1/2} \approx 2.5$. For comparison, the results of our numerical simulations are shown in Figure 10 for D = 1.8 cm, and an initial density difference of 5%. The circulation is defined as the vorticity flux for r less than 1.41 standard deviations [exp(-1)] of the normalized vorticity contour (normalized by the local maximum vorticity). It was found that as the aspect ratio decreased, the asymptotic circulation also decreased. The minimum normalized circulation was about 1.6 with L/D = 0.25 and the maximum

was around 2.6 with L/D >2, the latter being in the range found by Bond and Johari (2005). Meanwhile, when the initial density differences was changed to 1% and 10% with L/D = 2, only minor effects on the circulation (order of 10%) were observed (not shown here).

3.5 Discussion

3.5.1 Comparison with Hill's spherical vortex

It is worth comparing the numerical results with results from classical analytical descriptions of round thermals. Hill (1894) provided a simple, if approximate, model of a spherical vortex, and Turner (1964) proposed using an expanding Hill's spherical vortex to model the flow field induced by a round thermal. Lai et al. (2013) demonstrated some success using an expanding Hill's spherical vortex to model a two-phase particle thermal.

For a Hill's vortex translating at speed U with radius a centered at (0, 0), the vortex induced velocity field relative to a stationary observer is given by (e.g. Turner 1964):

Inside the entrained fluid [$R<a$, $R = (r^2+z^2)^{1/2}$]:

$$u_z = -\frac{3U}{4}[4(\frac{r}{a})^2 + 2(\frac{z}{a})^2 - \frac{10}{3}] \tag{8}$$

$$u_r = \frac{3U}{2a^2} rz \tag{9}$$

Outside the entrained fluid ($R>a$):

$$u_z = \frac{Ua^3}{2} \frac{2z^2 - r^2}{(z^2 + r^2)^{5/2}} \tag{10}$$

$$u_r = \frac{3Ua^3 rz}{2(z^2 + r^2)^{5/2}} \tag{11}$$

The flow field given by Equations (8) – (11) was first compared with the numerical results induced by a thermal with $L/D = 2$ and initial density difference of 5%. As shown in Figure 11(a), the characteristic radius a of the Hill's vortex was taken as the maximum radius of the thermal, while the characteristic velocity U as the rise velocity of the thermal vortex ring dz_r/dt at that particular time instance. The transects used for comparing velocity profiles are indicated as dashed lines in Figure 11(a). Figure 11(b) shows that the general flow pattern predicted by a Hill's vortex was close to the numerical simulations. Similarly, Figures 12 and 13 show good agreement with the vertical and radial velocities. However, the simulated vorticity distribution was somewhat different. We also compared (not shown) the Hill's vortex induced velocity with thermals of other aspect ratios which resulted in a thinner buoyant vortex ring. Hill's vortex, which is theoretically applicable to only thick ring vortex rings, was found to deviate further from the numerical simulation as the aspect ratio decreased. However, for engineering purposes, it can still give a fair prediction of flow field for an aspect ratio as low as $L/D = 0.5$. Further improvement in the way of analytical predictions can be expected if we adopt the Norbury vortex family of variable thickness, which is a general form of the Hill's vortex of variable ring core thickness. However, the Norbury vortex has no trivial solution to its induced flow and is thus less suitable for applications which require efficient solutions.

3.5.2 Sensitivity of $C_{3\varepsilon}$

The flow of a thermal is driven solely by its buoyancy, and thus it is expected that the buoyancy production of kinetic energy and the dissipation rate would both be important to the flow. As indicated early, the buoyancy associated coefficient, $C_{3\varepsilon}$, has to be estimated since it is dependent on the flow type (Rodi 1987). Here, we

varied $C_{3\varepsilon}$ for the case of D5LD2 as an example. While the resulting concentration contours did not yield significant difference, the spreading rate of the thermal was more sensitive. The spreading rate of the ring varied non-linearly from 0.13 – 0.25 as $C_{3\varepsilon}$ changed from 1.0 – 0.5. Similar to other coefficients in the k-ε model, $C_{3\varepsilon}$ requires calibration with experiments. In this study, $C_{3\varepsilon}$ was finally chosen to be 0.8 which gave reasonable predictions of thermal characteristics when compared to both Zhao et al. (2013)'s and Hart (2008)'s experiments in which L/D ranged from 0.5 to 2.0.

3.5.3 Sensitivity of grid size and physical domain size

We checked grid size convergence using a coarse grid of 100 x 300 cells, a medium grid of 150 x 450 cells, as well as the chosen 200 x 600 cell grid. Using the case of D5LD2 as an example, the coarse grid produced on average 1.8%, 3.2%, and 1.0% difference for the thermal radius, frontal position, and circulation respectively, when comparing to the fine grid. The difference reduced to 0.4%, 1.6%, and 0.5% respectively when the medium grid was adopted. The small differences suggested that the present grid resolution was sufficient.

Also, to ensure the physical domain used is sufficiently large with negligible boundary effects on the results, we doubled the width of the physical domain (to 0.30 m) and re-run selected numerical simulations; the difference of the spreading rate obtained is typically less than 5%.

3.5.4 Formation number of a thermal

The formation number (Gharib et al. 1998) relates to the maximum vorticity that can be incorporated into a vortex ring before the ring 'pinches off' from its trailing stem. It can thus be regarded as the maximum L/D of the injection/release without producing a trailing stem. Both the vortex ring and positively buoyant

vortex ring had been shown to have a formation number of about 4 – 5 (Gharib et al. 1998, Wang et al. 2009). Our numerical results showed that, for a thermal, the formation number is somewhat lower (L/D ≈ 2). (But also note that our formation number is defined using the maximum volume of fluid that can be incorporated into the vortex; while Gharib et al. 1998's definition is based on the maximum vorticity that can be incorporated.) This is in agreement with the observation from Bond and Johari (2005), who observed that for thermals, a structure similar to that of a starting plume will form for $L/D > 2$.

3.5.5 Impulse and buoyancy of a thermal

The impulse equation of Turner (1957) (see Equation 13 below) relates the rate of change of impulse, dI/dt, of the thermal to the buoyancy force acting on it. While the equation is reasonable, Bond and Johari (2005) observed that the rate of change of impulse was only equal to about 40% of the buoyancy force ($dI/dt \approx 0.4F$) for $L/D > 2$. The apparent loss of buoyancy can partly be explained by using the concept of formation number. For $L/D > 2$, only a portion of the initial buoyant fluid can be incorporated into the thermal, and thus the buoyancy of the thermal is less than the total buoyancy of the release. Our numerical results show that $dI/dt \approx F$ for $L/D < 2$, but only about 90% of buoyant fluid can be incorporated into the thermal for $L/D = 3$, and only about 80% for $L/D = 4$. Thus, the impulse-buoyancy relationship no longer holds if pinch-off occurs. The buoyancy in the thermal is expected to further decrease for higher L/D. Other possible reasons for the observed smaller change in impulse were suggested in Bond and Johari (2005). Hence, for Equation (13) to be valid, it is necessary to ensure the initial release condition of $L/D < 2$ for the thermal.

4 A model for predicting thermal spreading rate

The above results from the numerical simulations showed that a lower aspect ratio leads to a higher thermal spreading rate. A predictive model of the spreading rate as a function of initial aspect ratio will be developed in this section using the buoyant vortex ring theory, and the Norbury vortex ring assumption.

4.1 Buoyant vortex ring theory

A thermal can be treated as a buoyant vortex ring without initial momentum. To predict the growth of a buoyant vortex ring, Turner (1957) used the vortex impulse (I) equation and assumed the circulation Γ of the ring to remain constant:

$$I = \pi\rho K r_r^{\,2} \tag{12}$$

$$\Rightarrow \frac{dI}{dt} = \pi\rho K \frac{dr_r^{\,2}}{dt} = gV(\rho_a - \rho) \tag{13}$$

$$\Rightarrow \frac{dr_r}{dz_r} = \alpha_r = \frac{F}{2\pi K}\frac{1}{r_r v} \tag{14}$$

In the above equations, V is the volume of the fluid carried by the vortex ring, $F = gV(\rho_a-\rho)$, and v is the vortex ring velocity.

With the assumption of self-similarity $v = cK/r_r$, where c is a constant, can be expressed as a function of the relative size between r_r and a (the ring core radius). Subsequently, the growth rate of a thermal can then be expressed as:

$$\alpha_r = \frac{1}{2\pi c(K/F^{1/2})^2} \tag{15}$$

4.2 Prediction of *c* using the Norbury vortex family

From Equation (15), in order to predict the growth of the thermal, it is necessary to determine c, which relates to the thermal's shape, and the thermal's normalized circulation $K/F^{1/2}$. There exist some special steady vortex ring solutions that can enable c to be predicted. Turner (1957) illustrated the two examples of Lamb's thin ring vortex and Hill's spherical vortex as follows:

$$c = \begin{cases} \frac{1}{4\pi}\{\ln(\frac{8R}{a}) - \frac{1}{4}\} & \text{Lamb's thin ring vortex} \\ \frac{1}{5}\sqrt{\frac{2}{5}} & \text{Hill's spherical vortex} \end{cases} \quad (16)$$

These two solutions represent the extremes of a thin and a thick vortex ring core. From this study, however, the vortex ring core size is intrinsically related to the initial aspect ratio of the cylindrical fluid. Thus, we propose instead using the Norbury vortex family to represent the thermal as follows.

Using the second-order solution of Fraenkel (1972) for the Nobury vortex, we have:

$$c = \frac{1}{\pi}(1 + \frac{3}{4}E^2)\{[\frac{1}{4}\ln(\frac{8}{E}) - \frac{1}{16}] + E^2[-\frac{3}{32}\ln(\frac{8}{E}) + \frac{15}{128}]\} \quad (17)$$

where $E \approx$ (area of core)/(r_r^2) is the non-dimensional mean core radius.

If the relationship between E and L/D is established, c can then be expressed as a function of L/D. This relationship can be obtained using Linden and Turner (2001)'s approach by matching the circulation, impulse, and energy of the Norbury vortex and the cylindrical fluid using a slug model, with the modifications which account for the variable thermal exit velocity with time.

We first assume that close to the source, the circulation of a thermal is mostly contributed by the boundary layer vorticity generated from the cylinder wall (similar to that of a vortex ring), with negligible baroclinic circulation generated. Second, we assume that the velocity *u* of the thermal increases linearly with time *t* from rest, i.e. $u = g't$; this is evident from the experimental thermal exit velocity by Bond and Johari (2005). With these, we can define an average velocity for the plug fluid which will be useful in later theoretical development:

$$\overline{U_p} = \frac{\int_0^T u dt}{T} = \frac{g'T}{2}, \quad L = \int_0^T u dt = \frac{g'T^2}{2} \tag{18}$$

$$\overline{U_p} L = 0.25 g'^2 T^3 \tag{19}$$

Now, the boundary layer generated circulation of the plug fluid is (Didden 1979)

$$K_p = (1.14 + \frac{0.32}{L/D}) \int_0^T \frac{1}{2} u^2 dt = \frac{2}{3}(1.14 + \frac{0.32}{L/D})(\overline{U_p} L) = k \overline{U_p} L$$

where

$k = \frac{2}{3}(1.14 + \frac{0.32}{L/D})$ being valid for L/D $\geq$ 0.6.

For L/D <0.6, we adopt $k = \frac{2}{3}[1.41(\frac{L}{D})^{-2/3}]$ (Pullin 1979).

Also, the plug fluid impulse is

$$P_P = \int_0^T u(u \frac{\pi D^2}{4}) dt = \frac{4}{3} V_o \overline{U_p} \tag{20}$$

and kinetic energy

$$T_P = \int_0^T \frac{1}{2} u^2 (u \frac{\pi D^2}{4}) dt = V_o \overline{U_p}^2 \tag{21}$$

Matching the circulation, impulse, and energy of the buoyant fluid to that of a Norbury vortex:

$$Ur_r K_R = k\overline{U_p}L \tag{22}$$

$$Ur_r^3 P_R = \frac{1}{3}\pi\overline{U_p}D^2 L \tag{23}$$

$$U^2 r_r^3 T_R = \frac{1}{4}\pi\overline{U_p}^2 D^2 L \tag{24}$$

K_R, P_R, T_R are the non-dimensional circulation, impulse, and energy respectively. Therefore, we have assumed that in this initial stage the mechanism for circulation is similar to that of a vortex sheet roll-up, and the circulation changes due to buoyancy only after the thermal formation. Details of the matching can be found in Linden and Turner (2001). The relationship of L/D and E is then:

$$\frac{L}{D} = \frac{1}{k^{3/2}}\sqrt{\frac{3\pi}{16}}\frac{P_R^{1/2} K_R^{3/2}}{T_R} \tag{25}$$

Vales of K_R, P_R, T_R can be obtained in Norbury (1973) for $E > 0.2$. For $E < 0.2$ we use the Fraenkel (1972)'s approximation to obtain K_R, P_R, T_R:

$$K_R = \pi \tag{26}$$

$$P_R = \pi^2(1+\frac{3}{4}E^2) \tag{27}$$

$$T_R = \pi^2\{[\frac{1}{2}\ln(\frac{8}{E}) - \frac{7}{8}] + \frac{3}{16}E^2\ln(\frac{8}{E})]\} \tag{28}$$

The resulting relationship of L/D and E is shown in Figure 14, which illustrates the intuitively correct result that a higher L/D yields a thicker vortex ring. For the thickest ring in the Norbury vortex family (the Hill's vortex) with $E = 2^{1/2}$, we obtain the maximum L/D of about 5, which is somewhat larger than the numerical observations. An alternative way of defining the formation number is to determine the L/D in which the maximum volume of fluid can be incorporated into the vortex head (Linden and Turner 2001). Adopting this definition and using

Linden and Turner (2001)'s approach, we obtain

$$\frac{\text{volume of vortex head}}{V_o} = \frac{16}{9}\frac{T_R}{P_R{}^2}(V_c + V_e) \tag{29}$$

where V_c and V_e are the volume of the vortex core and the irrotational fluid being carried by the vortex head respectively. As can be seen in Figure 15, this ratio is >1 for $E < 0.22$, while beyond 0.22 the ratio is <1 meaning that some of the fluid cannot be incorporated into the vortex head. The corresponding L/D with $E = 0.22$ is about 1.7, which can be regarded as the formation number; this is close to the numerical observation, in which the formation number is in fact defined in terms of fluid volume.

4.3 Prediction of normalized circulation

The normalized circulation $K/F^{1/2}$ in the 'far-field' (further from the source) had been shown to be approximately 2.5 for a thermal (Bond and Johari 2005, Zhao et al. 2013) with the specific aspect ratio of 2. For other aspect ratios, the thermal circulation was computed numerically and shown in Figure 10. It can in general be expressed as a function of the initial conditions of the cylindrical buoyant fluid as follows:

$$K = f(g\frac{\Delta\rho}{\rho_a}, L, D) \tag{30}$$

By dimensional analysis, we have:

$$\frac{K}{\sqrt{2g(\Delta\rho/\rho)}D^{3/2}} = \frac{K}{\sqrt{2g(\Delta\rho/\rho)D}L(D/L)} = f(\frac{L}{D}) \Rightarrow \frac{K}{\sqrt{2g(\Delta\rho/\rho)DL}} = f(\frac{L}{D}) \tag{31}$$

Note that the equation is cast into a form such that the circulation is normalized by a velocity scale $[2g(\Delta\rho/\rho)D]^{1/2}$ and a length scale L. The functional form of Equation (31) can be determined from the results of the numerical simulations (Figure 16) which suggest:

$$\frac{K}{\sqrt{2g(\Delta\rho/\rho)DL}} = 1.27\left(\frac{L}{D}\right)^{-0.175} \quad (32)$$

It can be seen that the sharpest change occurs for $L/D < 0.5$.

4.4 Prediction of thermal spreading rate

The vortex ring spreading rate (α_r) of the thermal can now be predicted using Equation (15), with c predicted by Equation (17) and the circulation by Equation (32). The predictions of the spreading rate are compared with numerical predictions in Figure 17, in which additional experimental data from previous investigations are also plotted. A factor of 1.40, which was the average obtained from numerical simulations, was used to convert the spreading rate of a buoyant vortex ring to that of thermal (α_m) (characterized by its maximum radius) in the predictions. A factor of 1.11 was found to relate this spreading rate, which used the height of the thermal concentration maximum, to the experimental and numerical data, which used the height of the thermal front in defining spreading rate (α_e). The prediction given by Equation (15) was valid up to $L/D = 1.7$, beyond which it was assumed that there was no further change on the spreading rate for the reason explained earlier. For the experimental data, although experimental variability existed in individual studies, a general trend of higher initial aspect ratio leading to smaller spread angle was evident. The minimum spread angle was obtained at $L/D \approx 2$, after which there was no further reduction. This can be seen in Turner (1973) and Diez et al. (2003)'s data of a starting plume, which effectively represents the case for an infinite L/D ratio.

5 Conclusions

The spreading rate of the thermal with different initial conditions has been investigated numerically in a systematic manner. The initial aspect ratio is found

to be a key factor affecting the thermal spreading rate. As the initial aspect ratio increases from 0.125 – 2.0, the resulting buoyant vortex ring core size increases, leading to direct changes in thermal characteristics. Beyond the aspect ratio of roughly 2 (i.e. the formation number), no further buoyant fluid can be incorporated into the vortex head and no further change is possible. The numerical results showed that as the aspect ratio increases from 0.125 to 2.0, the spreading rate of the thermal decreases from 0.31 to 0.13, which are roughly the upper and lower limits of observed values reported in the literature.

An analytical model was then developed to predict the spreading rate of a thermal with a given initial aspect ratio. First, assuming the plug fluid is accelerated by the reduced gravity, its initial circulation, impulse, and kinetic energy can be matched to that of a Norbury vortex (Linden and Turner 2001). This results in a functional relationship between the aspect ratio and the vortex core size, and hence the vortex ring shape. Also, by using dimensional analysis and the numerical simulation results, the asymptotic normalized circulation as a function of initial aspect ratio can be established. Second, using the buoyant vortex ring theory of Turner (1957), a model can be developed using the analytical expression relating the vortex ring shape, asymptotic normalized circulation and the spreading rate. The model predicted spreading rate is generally in good agreement with the results from both the numerical simulations of this study and previous experimental data. This suggests that the key physics governing the spreading of a thermal are captured.

Finally, it should be noted that many other factors can also affect the spreading rate of a thermal, including the turbulence level in the background and the characteristics of the release mechanism (the rate of release, any asymmetries, etc). The present study did not explore all these factors, but rather identifies the

importance of the initial aspect ratio due to its role in the formation process. Reported thermal spreading rates varied greatly in previous studies. Instead of attributing the differences to experimental errors, the systematic numerical investigation here shows that the initial aspect ratio can be the key factor that led to the observed variations.

The theoretical model developed here can be used in practice to determine the spreading rate of a thermal for integral modeling purpose. We also discussed the applicability of Hill's vortex in approximating the thermal induced flow, and showed that it is a reasonable model to be used for engineering applications within a range of typical initial aspect ratios.

Acknowledgements

This research was supported by the National Research Foundation Singapore through the Singapore-MIT Alliance for Research and Technology's CENSAM IRG research programme.

References

1. Bond H and Johari H (2005). Effects of initial geometry on the development of thermals. Exp. Fluids 39 (3): 589–599.

2. Bond H and Johari H (2010). Impact of buoyancy on vortex ring development in the near field. Exp. Fluids 48 (5), 737–745.

3. Bush JWM, Thurber BA, Blanchette F (2003) Particle clouds in homogeneous and stratified environments. J Fluid Mech 489:29-54

4. Didden N (1979). On the formation of vortex rings: Rolling-up and production of circulation. J. Appl. Mech. Phys. (ZAMP) 30:101 – 116

5. Diez FJ, Sangras R, Faeth GM and Kwon OC (2003). Self-preserving properties of unsteady round buoyant turbulent plumes and thermals in still fluids. Journal of Heat Transfer 125: 821-830

6. Escudier MP, Maxworthy T (1973) On the motion of turbulent thermals. J Fluid Mech 61(3):541-552

7. Fraenkel LE (1972) Examples of steady vortex rings of small cross-secction in an ideal fluid. J Fluid Mech 51(1):119-135

8. Gharib M, Rambod E and Shariff K (1998) A universal time scale for vortex ring formation. J Fluid Mech 360: 121-140

9. Hart AC (2008) Interacting thermals. PhD thesis, Department of Applied Mathematics and Theoretical Physics, University of Cambridge.

10. Hill MJM (1894) On a spherical vortex. Philos Trans Roy Soc London Ser A 185:213-245

11. Jasak H (1996). Error analysis and estimation in the Finite Volume method with applications to fluid flows. PhD thesis, Department of Mechanical Engineering , Imperial College London.

12. Lai ACH, Zhao B, Law AWK and Adams EE (2013). Two-phase modeling of sediment clouds. Environmental Fluid Mechanics, 13(5): 435 – 463.

13. Launder BE and Spalding DB (1974). The numerical computation of turbulent flows. Computer methods in applied mech. and engrg., 3(2): 269 – 289

14. Lee JHW and Chu VH (2003) Turbulent Jets and Plumes: A Lagrangian Approach. Springer.

15. Li CW and Ma FX (2003) Large eddy simulation of diffusion of a buoyancy source in ambient water. Applied Mathematical Modelling 27(8): 649-663

16. Linden PF and Turner JS (2001). The formation of 'optimal' vortex rings, and the efficiency of propulsion devices. J Fluid Mech 427: 61 – 72

17. Lundgren TS, Yao J and Mansour NN (1992) Miscroburst modeling and scaling. J Fluid Mech 239: 461–488.

18. Maxworthy T (1974) Turbulent vortex rings. J Fluid Mech 64(2): 227-239

19. Morton BR, Taylor GI, Turner JS (1956) Turbulent gravitational convection from maintained and instantaneous sources. Proc R Soc. Lond A 234: 1-23

20. OpenFOAM Foundation (2010). OpenFOAM: The open source CFD toolbox – User Guide, Version 1.7.1.

21. Pullin DI (1979) Vortex ring formation at tube and orifice openings. Phys. Fluids. 22: 401 – 403

22. Rodi W (1987). Examples of calculation methods for flow and mixing in stratified fluids. Journal of Geophysical Research, 92(C5): 5305-5328

23. Ruggaber GJ (2000) The dynamics of particle clouds related to open-water sediment disposal. PhD Thesis, Department of Civil and Environmental Engineering, Massachusetts Institute of Technology

24. Ruggaber GJ and Adams EE, (2001) Dynamics of particle clouds related to open-water sediment disposal. Conference on Dredged Material Management: Options and Environmental Considerations. MIT Sea Grant College Program, Cambridge, MA.

25. Scorer RS (1957) Experiments on convection of isolated masses of buoyant fluid. J Fluid Mech 2(6):583-594

26. Turner JS (1957) Buoyant vortex ring. Proc. Roy. Soc. Lond. A. 239: 61-75

27. Turner JS (1963) The motion of buoyant elements in turbulent surroundings. J Fluid Mech 16(1):1-16

28. Turner JS (1964) The flow into an expanding spherical vortex. J Fluid Mech 18(2):195-208

29. Turner JS (1973) Buoynacy effects in fluids. Cambridge University Press

30. Wang RQ, Law AWK, Adams EE and Fringer OB (2009). Buoyant formation number of a starting buoyant jet. Physics of Fluids, 21: 125104

31. Weller HG, Tabor G, Jasak H and Fureby C (1998). A tensorial approach to cpmutational continuum mechanics using object-oriented techniques. Computers in Physics 12(6):620 – 631.

32. Woodward B. (1959) The motion in and around isolated thermals. Quarterly Journal of the Royal Meteorological Society, 85(364): 144-151.

33. Zhao B, Law AWK, Adams EE, Shao D, Huang Z (2012) Effect of air release height on the formation of sediment thermals in water. J. Hydraulic Research 50(5): 532-540

34. Zhao B, Law AWK, Lai ACH, Adams EE, (2013) On the internal vorticity and scalar concentration structures of miscible thermals. J Fluid Mech, 722, R5 doi:10.1017/jfm.2013.158

Figure 1: (a) Instantaneous cross-sectional view of a round thermal observed in a laser-induced fluorescence experiment for L/D = 2; (b) the corresponding thermal concentration distribution by ensemble averaging 84 identical experiments. (credit: Bing Zhao)

Figure 2: A positively buoyant round thermal

Figure 3: Setup of the physical domain, and the initial and boundary conditions for the numerical simulations

Figure 4: Comparison of numerical predicted results (line) and experimental results of the gross characteristics of a thermal with L/D = 0.5 (squares: Hart 2008) and 2 (circles: Zhao et al. 2013) : (a) spreading rate; (b) transient height.

Figure 5: Comparison of numerical results using different initial density difference with L/D = 2: (a) thermal radius against time; (b) rise height against time

Figure 6: Comparison of numerical predicted results (line) and experimental results (symbols) of the internal structure of a thermal with L/D = 2 (Zhao et al. 2013): (a): concentration profile; (b) vorticity profile

Figure 7: (a) – (d): Normalized concentration contours of a round thermal with L/D = 0.5, 1.0, 2.0, and 3.0; (e) – (h): Normalized vorticity contours of a round thermal with L/D = 0.5, 1.0, 2.0, and 3.0.

Figure 8: (a) – (d): Normalized turbulent kinetic energy contours of a round thermal with L/D = 0.5, 1.0, 2.0, and 3.0; (e) – (h): Normalized turbulent kinetic energy dissipation contours of a round thermal with L/D = 0.5, 1.0, 2.0, and 3.0.

Figure 9: Thermal ring radius variation with height with different initial aspect ratio (a): $\Delta\rho/\rho$ = 3%, D = 3.7 cm; (b) $\Delta\rho/\rho$ = 5%, D = 1.8 cm; numerical data are plotted on 1 s interval

Figure 10: The effect of initial aspect ratio on the normalized circulation ($\Delta\rho/\rho$ = 5%).

Figure 11: Hill's vortex (circle) compared to the numerical simulated thermal of L/D =2: (a) size of thermal; (b) flow field induced by the thermal (blue: Hill's vortex, red: numerical simulation, *w* is the average vertical velocity within the normalized concentration contour of 0.2)

Figure 12: Comparison of the Hill's vortex induced (solid lines) and the numerically simulated (symbols) vertical velocity along the transects defined in figure 11(a).

Figure 13: Comparison of the Hill's vortex induced (solid lines) and the numerically simulated (symbols) radial velocity along the transects defined in figure 11(a).

Figure 14: Non-dimensional vortex core size *E* of a Norbury vortex as a function of aspect ratio *L*/*D*

Figure 15: The ratio of the plug fluid that can be carried by the vortex head against the non-dimensional vortex core size *E*

Figure 16: The normalized thermal circulation as a function of *L*/*D*.

Figure 17: Analytically predicted (dotted line: rise height defined at thermal front; solid line: rise height defined at thermal concentration maxima) and observed α of a thermal with different initial aspect ratios (open symbols: numerical results; closed symbols: experiments)

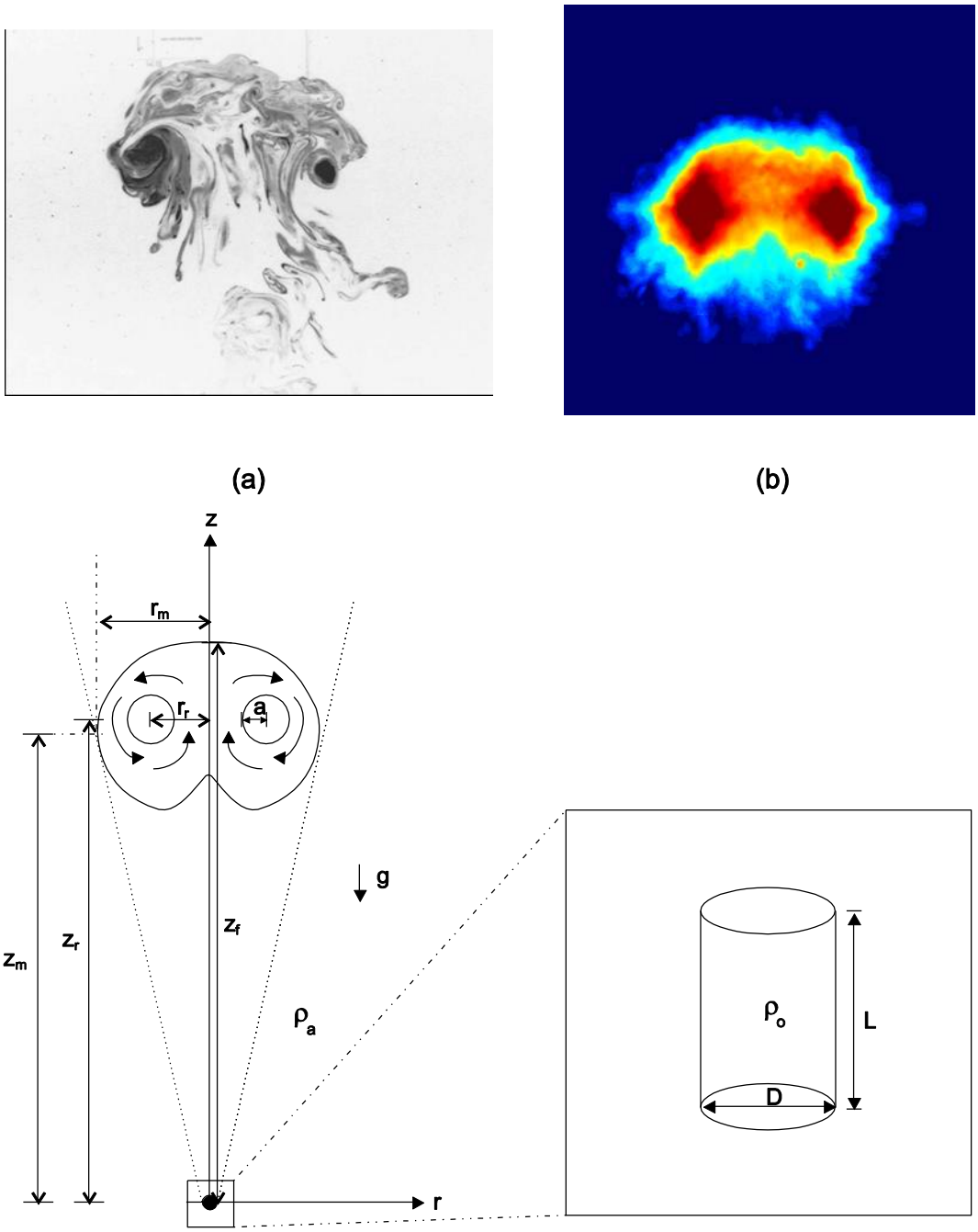
(a)
(b)
z
r_m
r_r
a
g
z_f
z_r
z_m
ρ_a
r
ρ_o
L
D

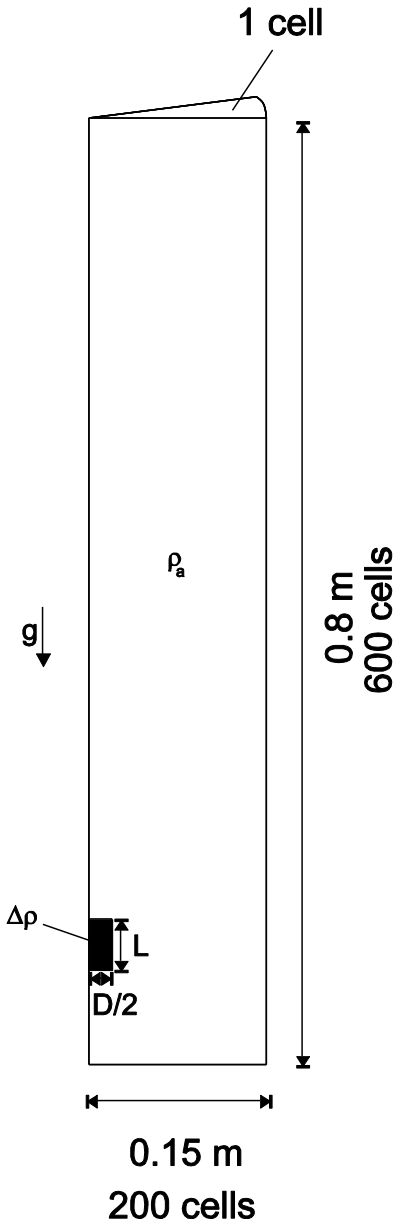
1 cell
ρ_a
g
0.8 m
600 cells
Δρ
L
D/2
0.15 m
200 cells

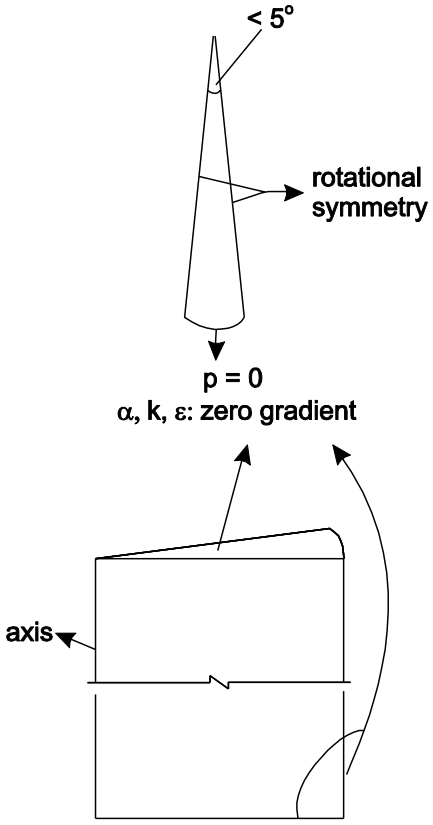
< 5°
rotational
symmetry
p = 0
α, k, ε: zero gradient
axis

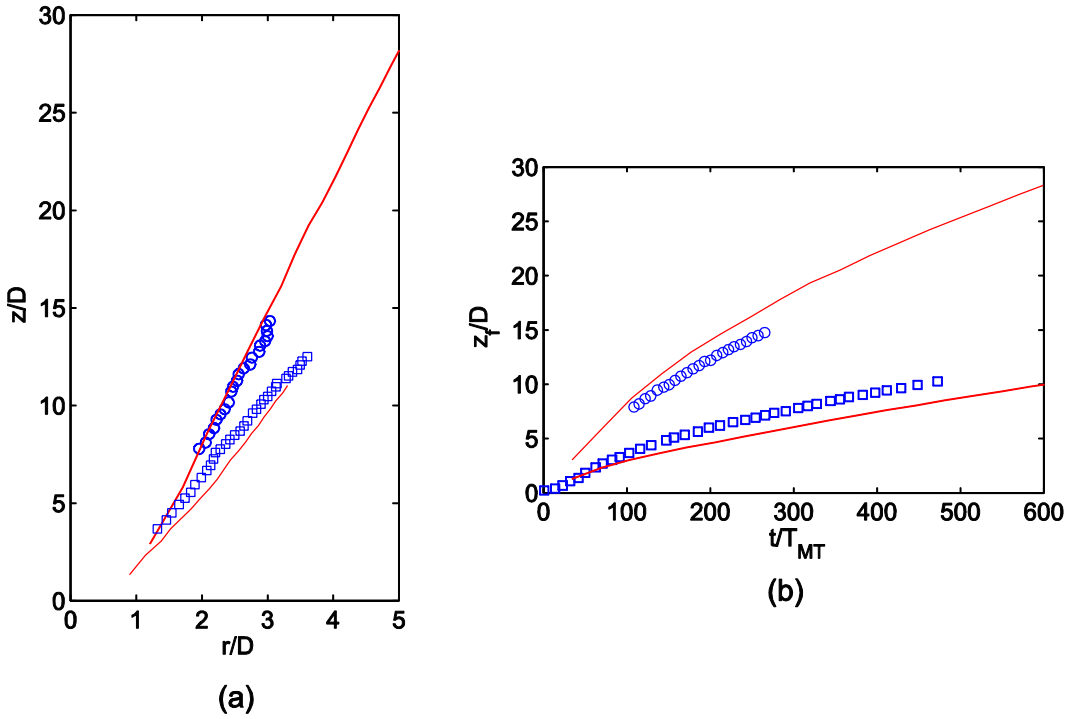
z/D
r/D
(a)
z_f/D
t/T_{MT}
(b)

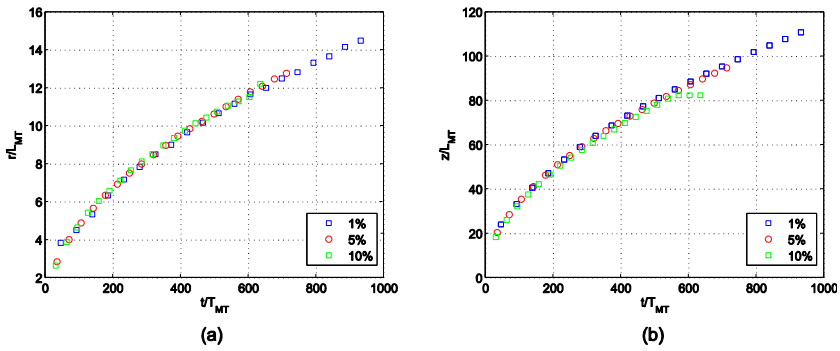
r/l_{MT}
z/l_{MT}
t/T_{MT}
1%
5%
10%
(a)
(b)

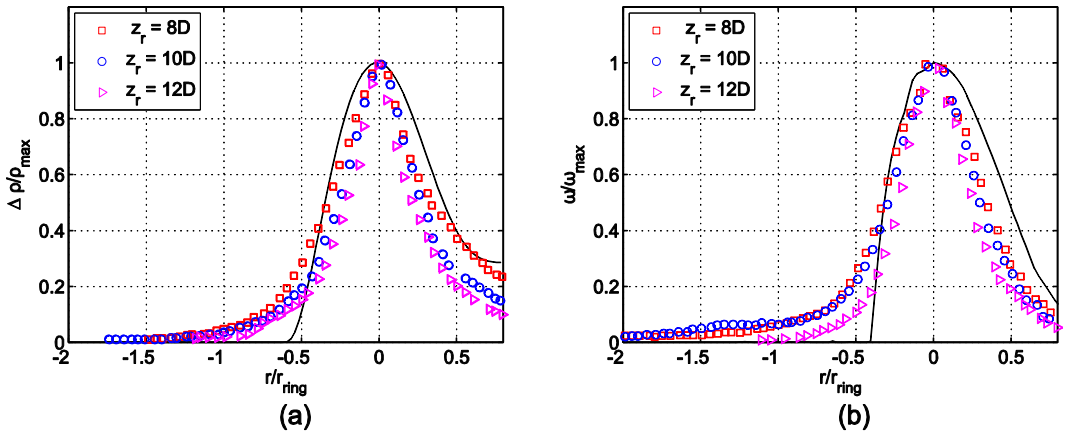
z_r = 8D
z_r = 10D
z_r = 12D
Δ ρ/ρmax
ω/ωmax
r/r_ring
(a)
(b)

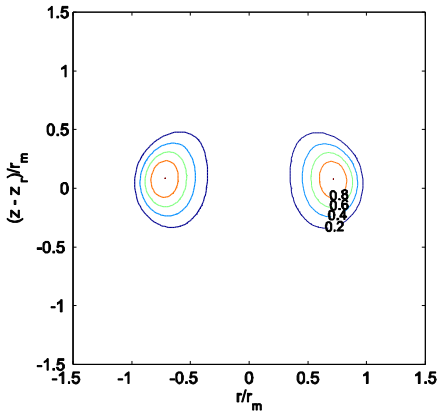
1.5
1
0.5
0
-0.5
-1
-1.5
-1.5 -1 -0.5 0 0.5 1 1.5
(z - z_r)/r_m
r/r_m
0.8
0.6
0.4
0.2

(a)

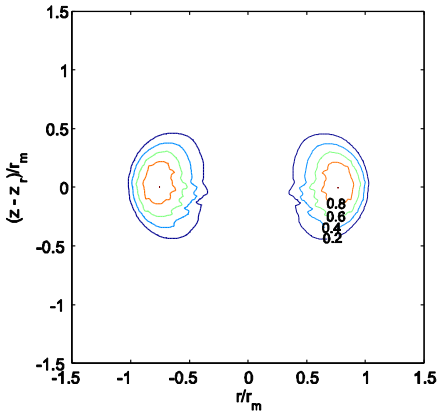
1.5
1
0.5
0
-0.5
-1
-1.5
-1.5 -1 -0.5 0 0.5 1 1.5
(z - z_r)/r_m
r/r_m
0.8
0.6
0.4
0.2

(e)

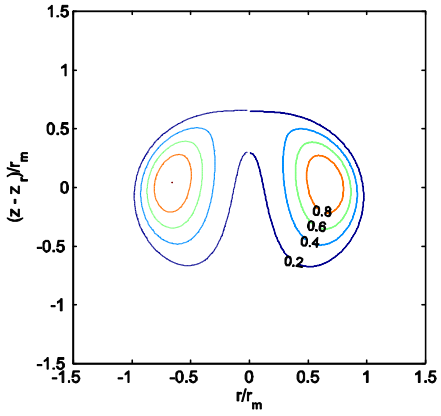
1.5
1
0.5
0
-0.5
-1
-1.5
-1.5 -1 -0.5 0 0.5 1 1.5
(z - z_r)/r_m
r/r_m
0.8
0.6
0.4
0.2

(b)

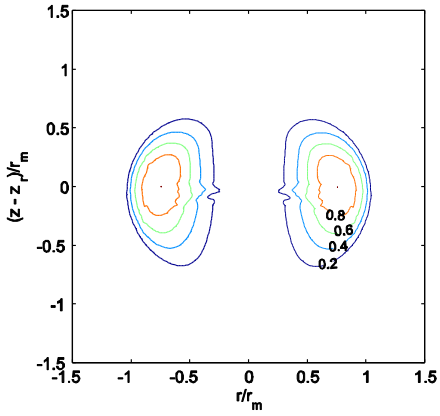
1.5
1
0.5
0
-0.5
-1
-1.5
-1.5 -1 -0.5 0 0.5 1 1.5
(z - z_r)/r_m
r/r_m
0.8
0.6
0.4
0.2

(f)

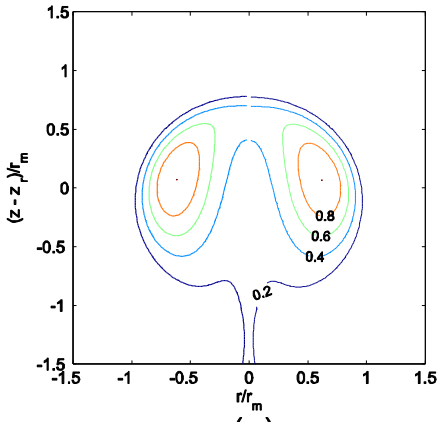
1.5
1
0.5
0
-0.5
-1
-1.5
-1.5 -1 -0.5 0 0.5 1 1.5
(z - z_r)/r_m
r/r_m
0.8
0.6
0.4
0.2

(c)

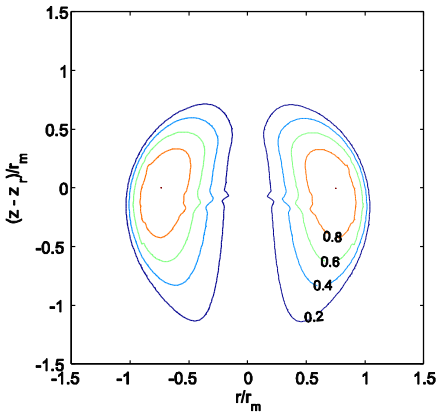
1.5
1
0.5
0
-0.5
-1
-1.5
-1.5 -1 -0.5 0 0.5 1 1.5
(z - z_r)/r_m
r/r_m
0.8
0.6
0.4
0.2

(g)

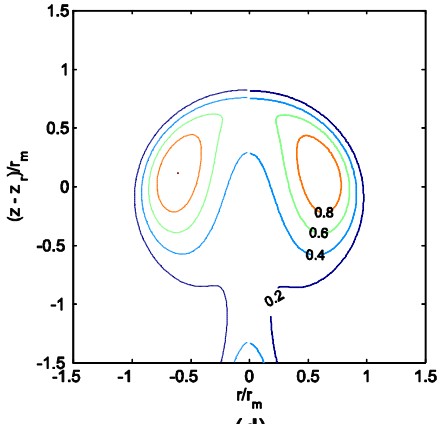
1.5
1
0.5
0
-0.5
-1
-1.5
-1.5 -1 -0.5 0 0.5 1 1.5
(z - z_r)/r_m
r/r_m
0.8
0.6
0.4
0.2

(d)

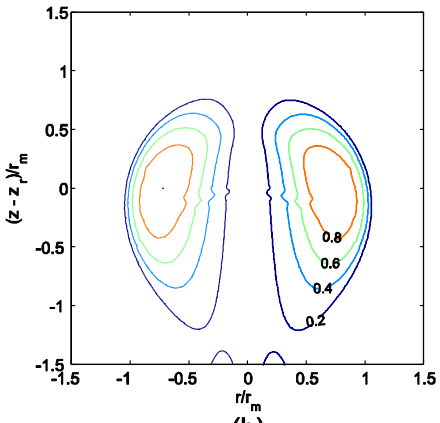
1.5
1
0.5
0
-0.5
-1
-1.5
-1.5 -1 -0.5 0 0.5 1 1.5
(z - z_r)/r_m
r/r_m
0.8
0.6
0.4
0.2

(h)

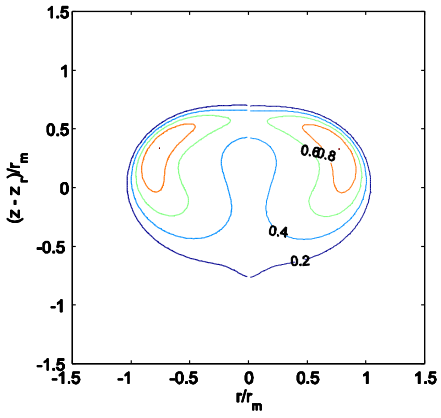
1.5
1
0.5
0
-0.5
-1
-1.5
-1.5 -1 -0.5 0 0.5 1 1.5
(z - z_r)/r_m
r/r_m
0.8
0.6
0.4
0.2

(a)

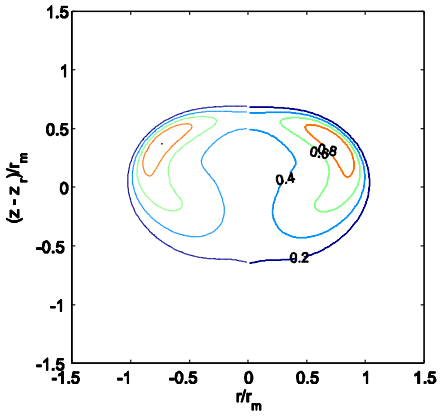
1.5
1
0.5
0
-0.5
-1
-1.5
-1.5 -1 -0.5 0 0.5 1 1.5
(z - z_r)/r_m
r/r_m
0.8
0.4
0.2

(e)

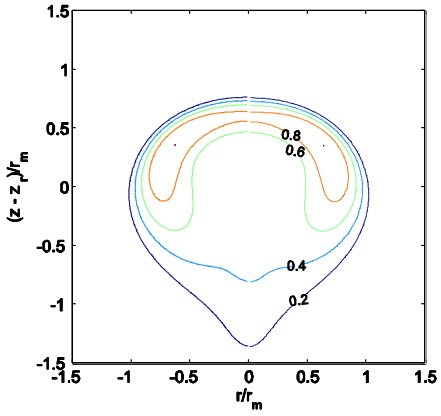
1.5
1
0.5
0
-0.5
-1
-1.5
-1.5 -1 -0.5 0 0.5 1 1.5
(z - z_r)/r_m
r/r_m
0.8
0.6
0.4
0.2

(b)

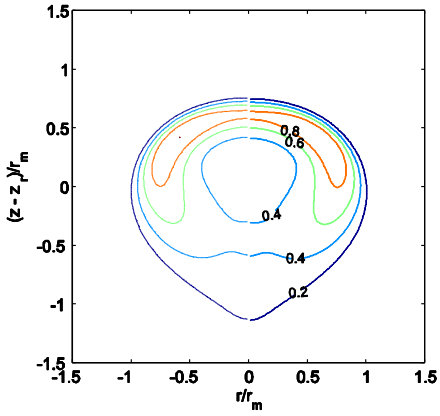
1.5
1
0.5
0
-0.5
-1
-1.5
-1.5 -1 -0.5 0 0.5 1 1.5
(z - z_r)/r_m
r/r_m
0.8
0.6
0.4
0.4
0.2

(f)

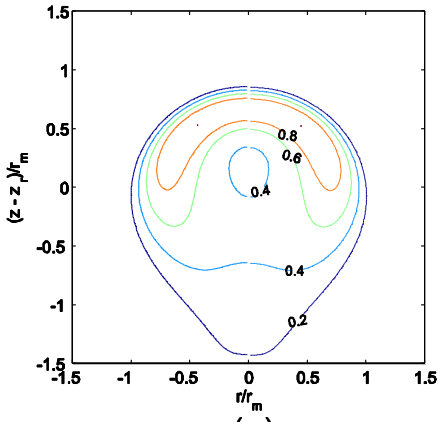
1.5
1
0.5
0
-0.5
-1
-1.5
-1.5 -1 -0.5 0 0.5 1 1.5
(z - z_r)/r_m
r/r_m
0.8
0.6
0.4
0.4
0.2

(c)

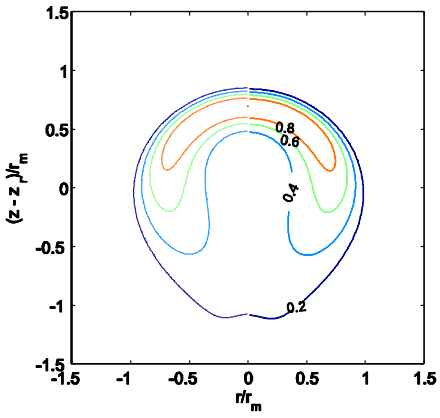
1.5
1
0.5
0
-0.5
-1
-1.5
-1.5 -1 -0.5 0 0.5 1 1.5
(z - z_r)/r_m
r/r_m
0.8
0.6
0.4
0.2

(g)

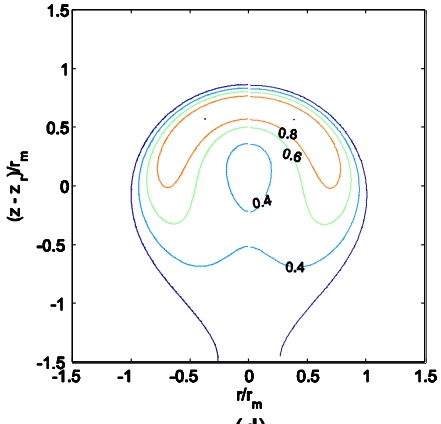
1.5
1
0.5
0
-0.5
-1
-1.5
-1.5 -1 -0.5 0 0.5 1 1.5
(z - z_r)/r_m
r/r_m
0.8
0.6
0.4
0.4

(d)

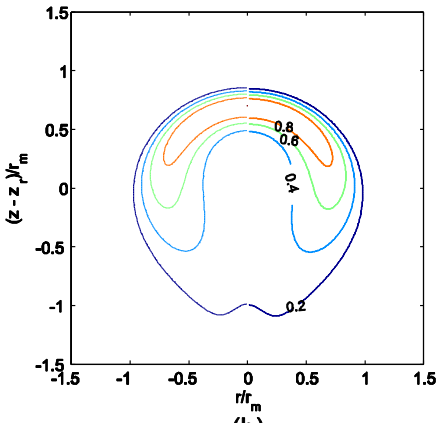
1.5
1
0.5
0
-0.5
-1
-1.5
-1.5 -1 -0.5 0 0.5 1 1.5
(z - z_r)/r_m
r/r_m
0.8
0.6
0.4
0.2

(h)

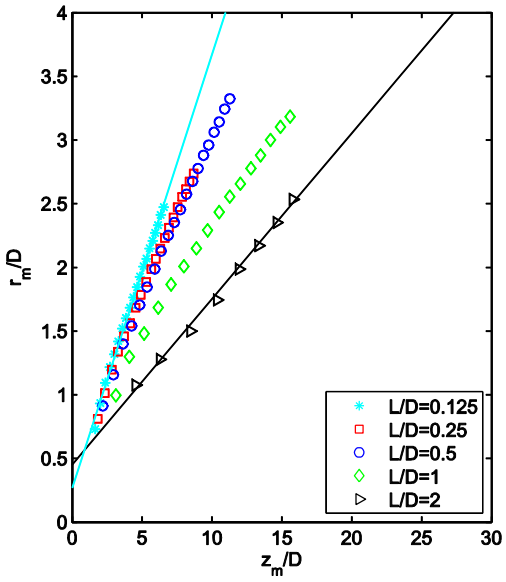
r_m/D
z_m/D
L/D=0.125
L/D=0.25
L/D=0.5
L/D=1
L/D=2

(a)

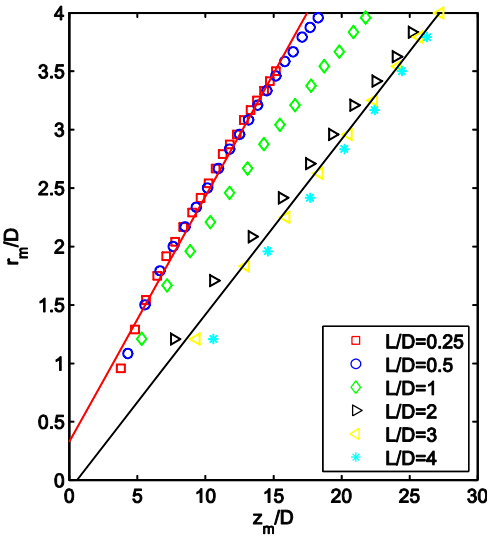
r_m/D
z_m/D
L/D=0.25
L/D=0.5
L/D=1
L/D=2
L/D=3
L/D=4

(b)

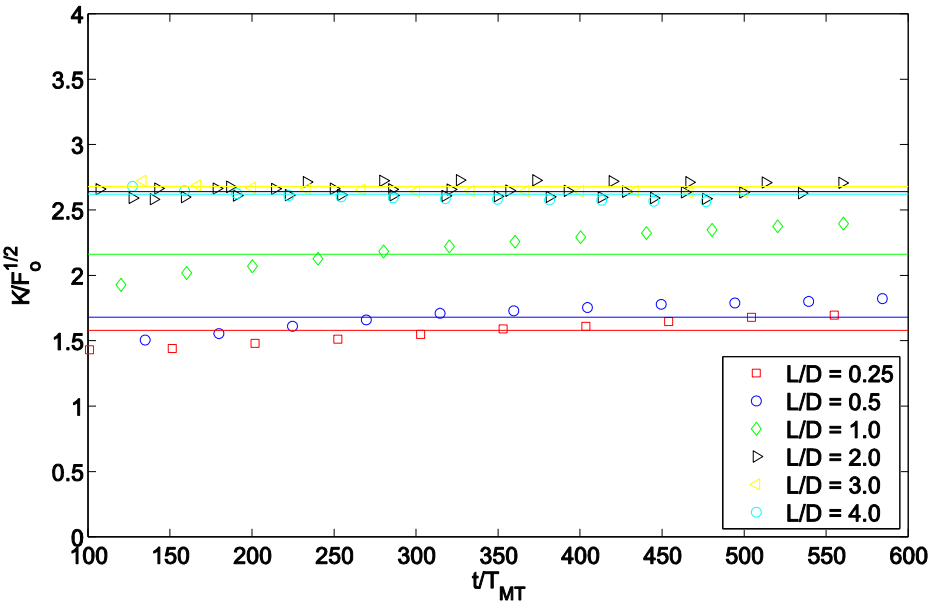
K/F_o^1/2
t/T_MT
L/D = 0.25
L/D = 0.5
L/D = 1.0
L/D = 2.0
L/D = 3.0
L/D = 4.0

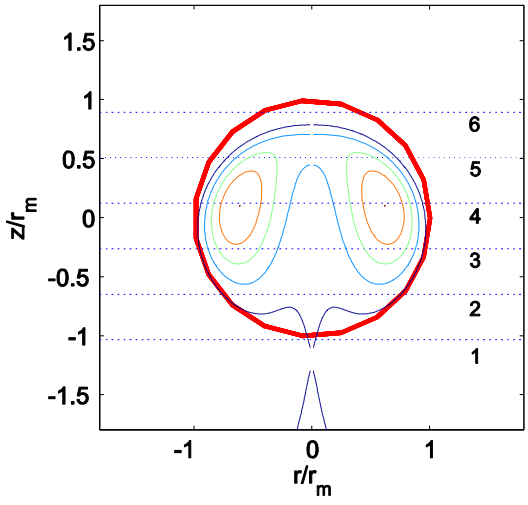
z/r_m
r/r_m
6
5
4
3
2
1

(a)

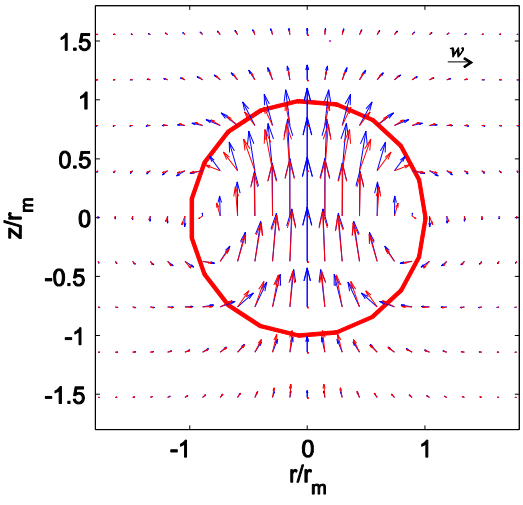
z/r_m
r/r_m
w

(b)

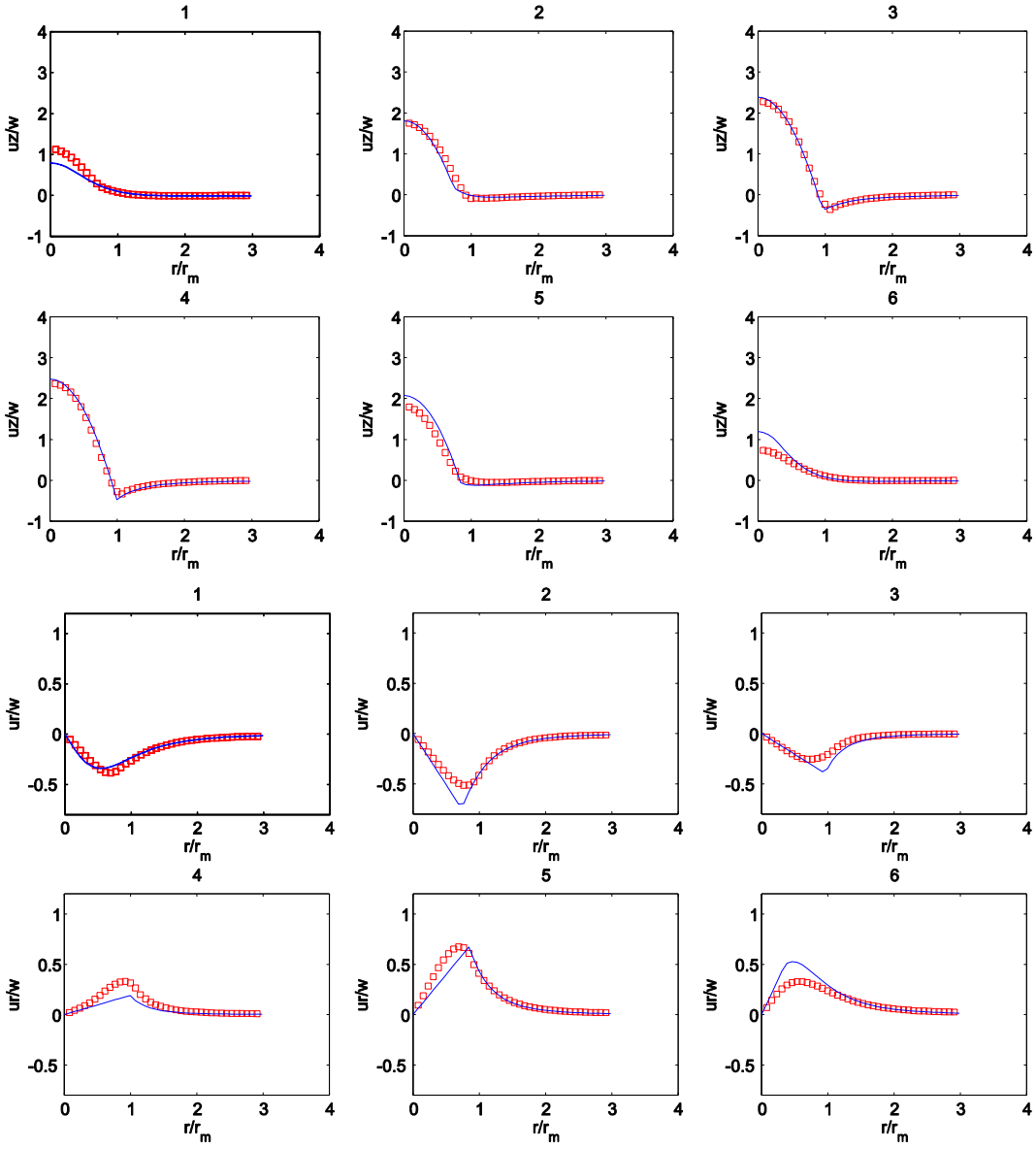
1
2
3
4
5
6
uz/w
ur/w
r/r_m

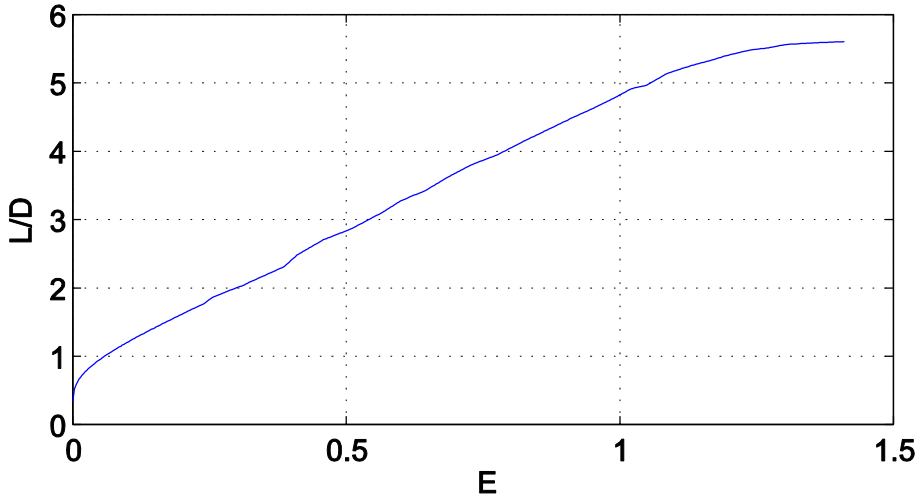
L/D
E
0
0.5
1
1.5
2
3
4
5
6

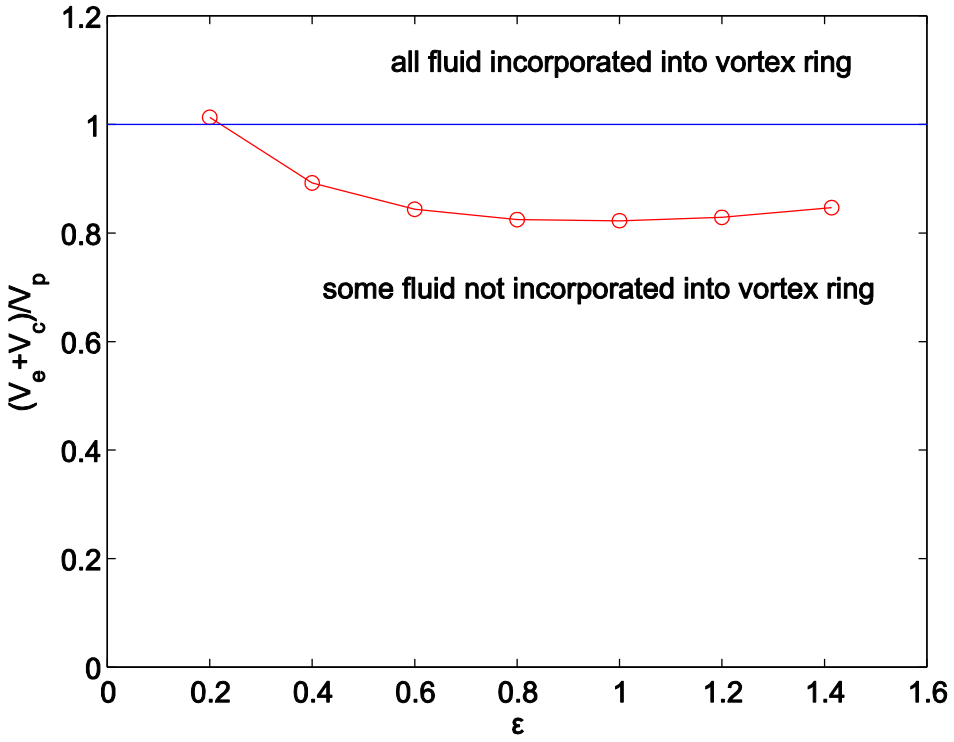
all fluid incorporated into vortex ring
some fluid not incorporated into vortex ring
$(V_e+V_c)/V_p$
ε
1.2
1
0.8
0.6
0.4
0.2
0
0
0.2
0.4
0.6
0.8
1
1.2
1.4
1.6

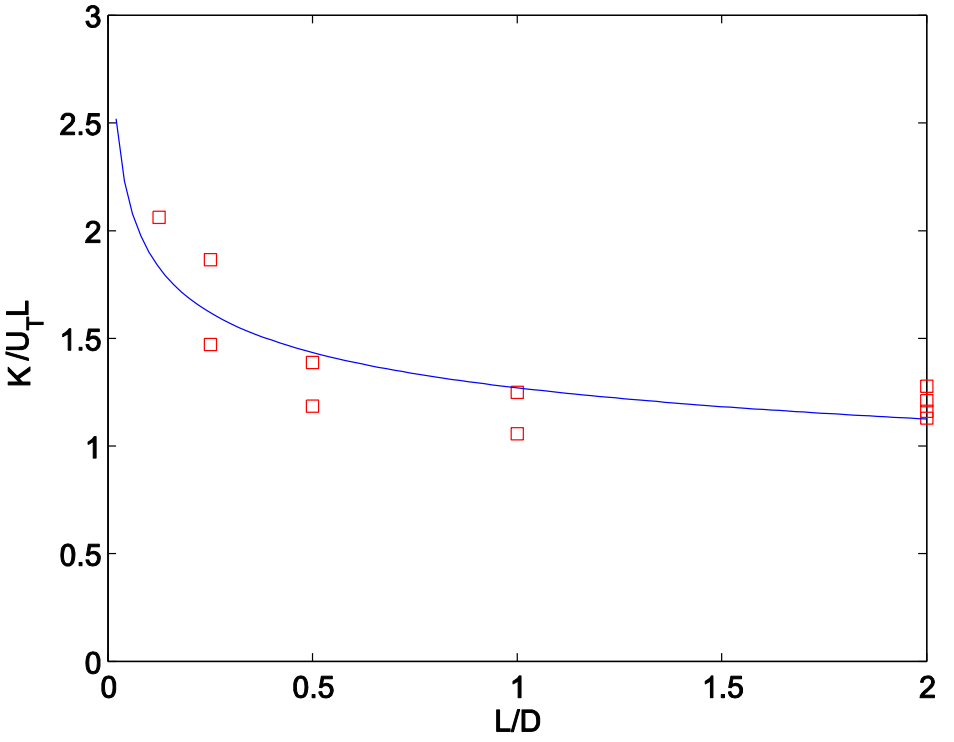
K/U_TL
L/D
3
2.5
2
1.5
1
0.5
0
0
0.5
1
1.5
2

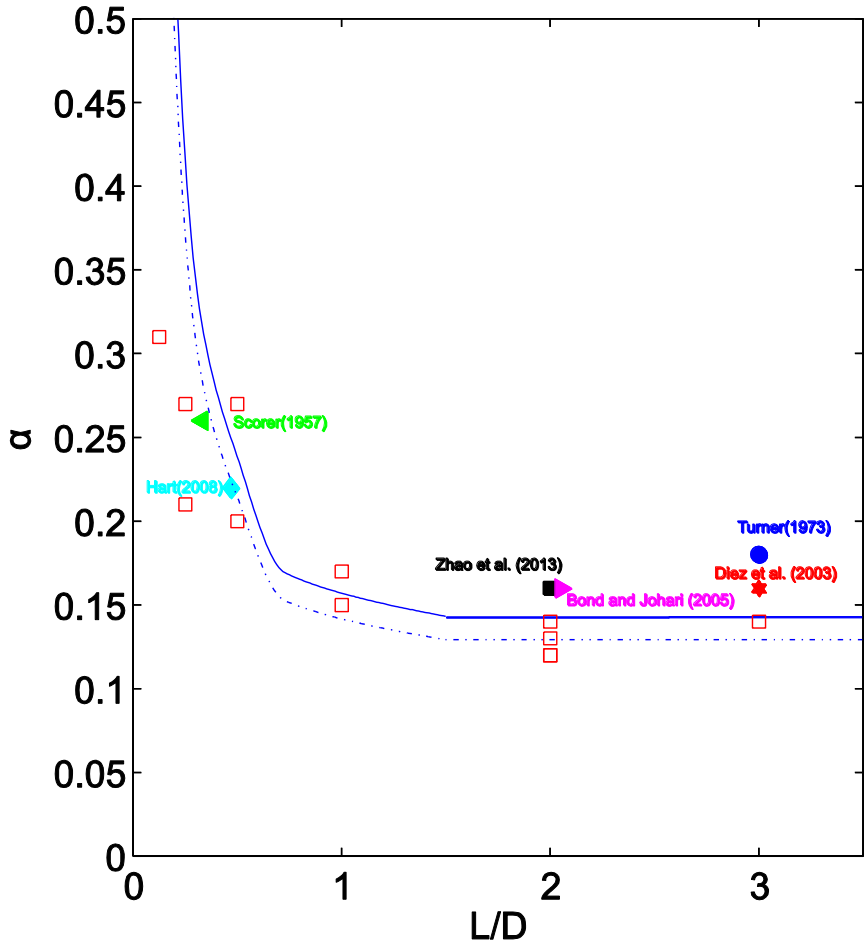

Case	L (cm)	D (cm)	L/D	Δρ/ρ
D5LD025	0.45	1.8	0.25	5%
D5LD05	0.9	1.8	0.5	5%
D5LD1	1.8	1.8	1	5%
D5LD2	3.6	1.8	2	5%
D5LD3	5.4	1.8	3	5%
D5LD4	7.2	1.8	4	5%
D10LD2	3.6	1.8	2	10%
D1LD2	3.6	1.8	2	1%
D3LD0125	0.4625	3.7	0.125	3%
D3LD025	0.925	3.7	0.25	3%
D3LD05	1.78	3.7	~ 0.5	3%
D3LD1	3.7	3.7	1	3%
D3LD2	7.4	3.7	2	3%

Table 1: Release conditions of this numerical study